#### RESEARCH ARTICLE



### Applied Polymer WILEY

# High-throughput fabrication, structural characterization, and cellular interaction of compositionally diverse fish gelatin/polycaprolactone (PCL) nanofibrous materials

Hannah A. Lacy<sup>1</sup> | Věra Jenčová<sup>2</sup> | Šarká Hauzerová<sup>2</sup> | Andrei Stanishevsky<sup>1</sup> o

#### Correspondence

Andrei Stanishevsky, Department of Physics, University of Alabama at Birmingham, 310 Campbell Hall, 1300 University Boulevard, Birmingham, AL 35233, USA.

Email: astan@uab.edu

#### **Funding information**

National Science Foundation, Grant/Award Number: 1852207; U.S. Department of Education, Grant/Award Number: P200A180001

#### **Abstract**

Nanofibers made by blending natural and synthetic biopolymers have shown promise for better mechanical stability, ECM morphology mimicry, and cellular interaction of such materials. With the evolution of production methods of nanofibers, alternating field electrospinning (a.k.a. alternating current (AC) electrospinning) demonstrates a strong potential for scalable and sustainable fabrication of nanofibrous materials. This study focuses on AC-electrospinning of poorly miscible blends of gelatin from cold water fish skin (FGEL) and polycaprolactone (PCL) in a range of FGEL/PCL mass ratios from 0.9:0.1 to 0.4:0.6 in acetic acid single-solvent system. The nanofiber productivity rates of 7.8-19.0 g/h were obtained using a single 25 mm diameter dish-like spinneret, depending on the precursor composition. The resulting nanofibrous meshes had 94%-96% porosity and revealed the nanofibers with 200-750 nm diameters and smooth surface morphology. The results of FTIR, XRD, and water contact angle analyses have shown the effect of FGEL/PCL mass ratio on the changes in the material wettability, PCL crystallinity and orientation of PCL crystalline regions, and secondary structure of FGEL in as-spun and thermally crosslinked materials. Preliminary in vitro tests with 3 T3 mouse fibroblasts confirmed favorable and tunable cell attachment, proliferation, and spreading on all tested FGEL/PCL nanofibrous meshes.

#### KEYWORDS

AC electrospinning, biomaterial, gelatin, nanofibers, polycaprolactone

#### 1 | INTRODUCTION

Nanofibers remain at the forefront of materials research and design with widespread applications in industry, medicine, energy, and more.<sup>1–4</sup> Nanofibers made of many

natural and synthetic polymers have been proven particularly useful in the production of biomaterials, drug delivery systems, and tissue engineering. Synthetic polycaprolactone and natural gelatin have been used frequently as exemplary materials in this area. <sup>5,6</sup> Current

This is an open access article under the terms of the Creative Commons Attribution-NonCommercial-NoDerivs License, which permits use and distribution in any medium, provided the original work is properly cited, the use is non-commercial and no modifications or adaptations are made.

© 2023 The Authors. *Journal of Applied Polymer Science* published by Wiley Periodicals LLC.

<sup>&</sup>lt;sup>1</sup>Department of Physics, University of Alabama at Birmingham, Birmingham, Alabama, USA

<sup>&</sup>lt;sup>2</sup>Department of Chemistry, Technical University of Liberec, Liberec, Czech Republic

research has employed direct current (DC) electrospinning as a main production method for nanofibrous materials, including those made using the combinations of PCL and gelatin.<sup>7-9</sup> In light of some of the shortcomings of DC methods, alternating field electrospinning (AFES, a.k.a. alternating current (AC) electrospinning) has gained traction in recent years as a high-yield, sustainable approach to nanofiber production. Cyclic nature of nanofiber generation, often different precursor requirements than in DC electrospinning, and slowly propagating dense fibrous flows in AFES allow expansion of the possible polymeric precursor systems, handling approaches of the generated nanofibers, and structure and textural properties of the resulting nanofibrous materials. 10-13 Lawson et al. 14 have shown that AFES of PCL can efficiently work with acetic acid as the only solvent, or with multi-solvent systems based on mixtures of formic acid, acetic acid, and acetone, as demonstrated by Sivan et al. 15 The PCL nanofibers productivity rates between 1.0 and 12.4 g·h<sup>-1</sup> were obtained depending on the solvent system and applied AC voltage. Varying the process parameters, such as AC frequency and solvent system, allows for modification of the resulting PCL nanofibrous material characteristics like wettability, contact angle, density, alignment, and surface energy. 16,17 Similarly, Jirkovec et al. 18 demonstrated the AFES capability to produce animal gelatin nanofibers from acetic acid and mixed acetic acid-water-ethanol solvent-based precursors. Kennell et al. 19 demonstrated AFES of fish gelatin (FGEL) nanofibers at up to 12.6 g·h<sup>-1</sup> productivity by using water as the solvent. Thermally crosslinked AFES FGEL nanofibrous meshes demonstrated favorable cellular response in an in vitro study with tdTomato mice fibroblasts.

The present study explores the combination of fish gelatin and PCL in a single solvent system for efficient AFES production of blended nanofibrous mats for potential biomedical uses. As PCL and gelatin blends have been repeatedly reported to have poor miscibility, 20-22 the solvent system and process parameters are expected to play an enormous role in the fiber formation and the resulting material structure and properties. To the date, no detailed study on the AC electrospinning of blended FGEL/PCL nanofibrous materials in a broad range of FGEL/PCL mass ratios have been attempted. A thorough characterization of the precursor and AFES process parameters has been performed in this study. The produced FGEL/PCL nanofibrous materials were characterized by SEM, FTIR, X-ray diffraction, wettability and in vitro tests to investigate the precursor-process-structure-properties relationships in the nanofibrous materials with FGEL/PCL mass ratios from 0.9:0.1 to 0.6:0.4.

#### 2 | EXPERIMENTAL

#### 2.1 | Materials

Polycaprolactone (PCL, 80,000 MW, granules) and gelatin from cold water fish skin (FGEL, BioReagent, powder) were purchased from Sigma-Aldrich Inc., US. Other ingredients used in this study included acetic acid (AA, glacial 99 + %, Alfa Aesar, US), sodium acetate (NaAc, anhydrous 99%, Alfa Aesar, US), 3 T3 mouse fibroblasts (NIH/3 T3 Swiss Albino, ATCC, Czech Republic), Dulbecco's Modified Eagle's Medium (DMEM), fetal bovine serum (FBS), and penicillin/streptomycin/amphotericin B (all were acquired from Lonza, CH).

#### 2.2 | Precursor preparation

First, the 30 wt% FGEL solution was prepared in a mixture glacial AA (95 v%) and deionized (DI) water (5 v%). Next, the 20 wt% PCL solution was prepared in glacial AA alone. Each solution was magnetically stirred for several hours until clear, viscous liquids were obtained. These pristine FGEL and PCL precursor solutions were then mixed in different volumes and stirred to prepare the blended polymeric precursors with 0.9:0.1, 0.8:0.2, 0.7:0.3, 0.6:0.4, 0.5:0.5, and 0.4:0.6 FGEL/PCL mass ratios. Small amounts of sodium acetate (NaAc, 1 wt% with respect to total polymer mass) were added to each precursor during the stirring to adjust the electrical conductivity and viscosity of the precursors. <sup>14</sup>

## 2.3 | Precursor properties measurements

Precursor viscosity tests were completed using a HAAKE RotoVisco 1 viscometer by Thermo Scientific. Both constant shear rate and dynamic tests were conducted, with shear rate varied from 0 to  $1000~\rm s^{-1}$ . Apparent viscosity data acquired at  $100~\rm s^{-1}$  shear rate for 120 s for each precursor were used as the figure of merit. Approximately 8.2 mL of solution was used for each measurement completed using the liquid cylinder and cup configuration, and 0.2 mL of solution was used for each measurement completed using the liquid plate and probe configuration. Measurements were repeated three times for each sample and the average of each data set was obtained.

Electrical conductivity was determined using Eutech Instruments CON 510 Bench Conductivity meter. The measuring probe was placed in approximately 5 mL of each of the solutions and the steady-state values were recorded. An average was calculated using five recorded values from each solution.

## 2.4 | Electrospinning of FGEL/PCL nanofibrous materials

Fabrication of nanofibrous meshes was performed using a custom-built AFES apparatus operated at up to 40 kV rms AC sinusoidal voltages at 60 Hz.<sup>23</sup> FGEL/PCL precursor solutions were delivered to a Teflon-enclosed spinneret and spun at 25-33 kV rms AC voltage. Ambient temperature and relative humidity were kept within the ranges of 20-23°C and 35%-41%, respectively. Dish-like spinnerets with 12.5-25 mm diameters were typically used. The generated FGEL/PCL nanofibers were collected on a rotating cylindrical plastic collector with 100 mm diameter and located at 250 mm distance from the spinneret. The duration of the AFES process was set to form 0.1 to 2.2 mmthick FGEL/PCL nanofibrous meshes. Good uniformity of the mesh thickness was achieved typically within 15-20 cm mesh width. The precursor flow rate was adjusted for each precursor, spinneret size, and voltage to maintain a constant level of the fluid on the spinneret.

# 2.5 | Precursor solution flow and process productivity

The flow rate and production rate of the polymer precursor solutions was determined by individual measurement of the consumed volume ( $V_p$ , mL) of precursor solution and mass ( $m_{nf}$ , g) of the bulk nanofibers produced by AFES within a given timeframe. The volume of consumed precursor solution was determined using a syringe system that allows a controlled, measurable flow of precursor solution to the spinneret. The mass of the bulk nanofibers produced from the measured volume of the precursor solution was determined by collecting and removing the fibers for weighing performed with a Sartorius Entris<sup>®</sup> Analytical Balance. Flow rate ( $R_f$ , mL·min<sup>-1</sup>) and production rate ( $R_p$ , g·min<sup>-1</sup>) was then calculated using Equation (1) and (2), respectively, where t is the active time (in minutes) that electrospinning occurred.

$$R_{f} = \frac{V_{p}}{t} \tag{1}$$

$$R_p = \frac{m_{nf}}{t} \tag{2}$$

#### 2.6 | Crosslinking by heat treatment

The resulting FGEL/PCL nanofibrous meshes were thermally treated at 160°C for 4 h using either a Thermo Scientific Heratherm oven or Panasonic Dry Heat Sterilizer MOV-212S-PE to crosslink the material. The heat treatment

also served a dual purpose of sterilization for the meshes prior to use in cellular studies. To maintain sterility, the mesh samples intended for use in cellular studies were prepared, cut to size, and then heated within sterile sealed glass petri dishes so that they could be transferred to the cell seeding area. Other meshes not intended for cellular studies were heated on flexible fiberglass sheets and then removed for further characterization.

#### 2.7 | FTIR spectroscopy

Fourier transform infrared spectroscopy was performed using Bruker Vertex 70 FTIR Spectrometer (2 cm<sup>-1</sup> resolution) in transmission mode to characterize the functional groups of the bulk nanofibers prior to and after heat treatment. Samples were prepared with minimal thicknesses and affixed to the device holder with 8 mm aperture such that the infrared beam was able to pass through.

#### 2.8 | X-ray diffraction analysis

The Malvern PANalytical Empyrean X-ray diffractometer was used to perform X-ray diffraction (XRD) in transmission mode to determine the crystallinity of the prepared materials. Samples were cut into 16 mm circles of approximately 1 mm thickness and placed between thin mylar films secured to transmission sample holders before insertion into reflection-transmission spinner sample stage. Each test was performed in the range of 5–40°  $2\theta$  during 5 min acquisition time. The PCL crystalline domain mean sizes were determined from the FWHM of the peak corresponding to (110) plane using Scherrer equation and Scherrer constant k=0.94.

#### 2.9 | Porosity and wettability analysis

The porosity of the samples before and after heat treatment was determined by using the calculated density of each sample. Each sample was cut to the specified length, width, and thickness, and the sample's mass was determined. These values were used to calculate the sample density, which was then compared to the theoretical density of the bulk solid FGEL/PCL material of given composition to calculate the porosity.

Water contact angle (WCA) measurements were performed using the PGX+ Pocket Goniometer in dynamic mode following sample preparation and procedure guidelines as established by the PGX+ user manual. A water droplet with  $\sim$ 2 mm diameter was gently placed on the

10974628, 0, Downloaded from https://onlinelibrary.wiley.com/doi/10.1002/app.54376, Wiley Online Library on [03/07/2023]. See the Terms and Conditions (https://onlinelibrary.wiley.com/terms-and-conditions) on Wiley Online Library for rules of use; OA articles are governed by the applicable Creative Commons Licensea

surface of nanofibrous samples. The device camera captured the droplet's images at 80 images·s<sup>-1</sup>. The images were processed using the device software and a curve expressing the wetting, absorption, and spread of the water droplet as a function of time was produced.

#### 2.10 | Scanning electron microscopy

A scanning electron microscope (SEM, Quanta FEG 650 or Tescan, VEGA3 SB easy probe) were concurrently used at 15–20 kV accelerating voltage to acquire the secondary electron images of the prepared samples. Samples were sputter-coated with a few nm of Au-Pd alloy using a Denton Vacuum Desk II prior to the SEM images to reduce the surface charging. SEM images were analyzed using ImageJ software (NIH, Bethesda, USA) to assess the nanofiber uniformity, diameter, morphology, bundling and orientation.

#### 2.11 | Cellular studies

Cellular in vitro studies were conducted for 1, 3, 7, and 14 days using 3 T3 mouse fibroblasts in the concentration of  $1 \times 10^4$  per well in 24-well plates using the Dulbecco's Modified Eagle's Medium (DMEM) supplemented with 10% (v/v) fetal bovine serum (FBS) and 1% (v/v) penicillin/streptomycin/amphotericin B. Cells were cultured in an incubator (37°C, 5% CO<sub>2</sub>). The medium was changed three times a week, and the second passage was used for the in vitro experiments. Nanofibrous mesh samples used were cut into 1.5 cm diameter circles suitable for 24-well plates and then heat treated for crosslinking and sterilization as described in Section 2.6 above. Nanofibrous mesh samples with cells intended for SEM

imaging were washed twice with PBS prior to fixation to remove unattached cells. The meshes were then fixed with 2.5% glutaraldehyde, washed with PBS, and dried using ethanol at increasing percentages of 60, 70, 80, 90, 96, and 100 for 10 min each. The samples were placed on parafilm for final drying before being subjected to the preparation and imaging protocol outlined in Section 2.10 above. Cellular viability was assessed at 1, 3, 7, and 14 days using cell counting kit-8 (CCK8, Dojindo) following sample preparation and procedure methods outlined in the Dojindo manufacturer manual and in relation to cell plating density. These samples were then analyzed in a 96-well plate using the Tecan SPARK® Multimode Microplate Reader at 450 nm absorbance in correlation to the culture number of living cells. The resulting data output files were exported for manual statistical analysis.

#### 3 | RESULTS AND DISCUSSION

#### 3.1 | AFES of FGEL/PCL nanofibers

#### 3.1.1 | Precursor viscosity and conductivity

Viscosity and electrical conductivity are the most critical attributes of the polymer precursor solution in electrospinning. In the case of AFES FGEL/PCL, the precursor viscosity within the range of 250–350 mPa·s allowed the uniform flow of nanofibers to be produced from the surface of spinneret with FGEL and all tested blended FGEL/PCL precursors (Figure 1a,b). The pristine PCL precursor required at least 600 mPa·s viscosity for uniform flow of nanofibers to form. The deviation of the viscosity values from their expected gradual increase with higher PCL content in FGEL/PCL precursor can be the

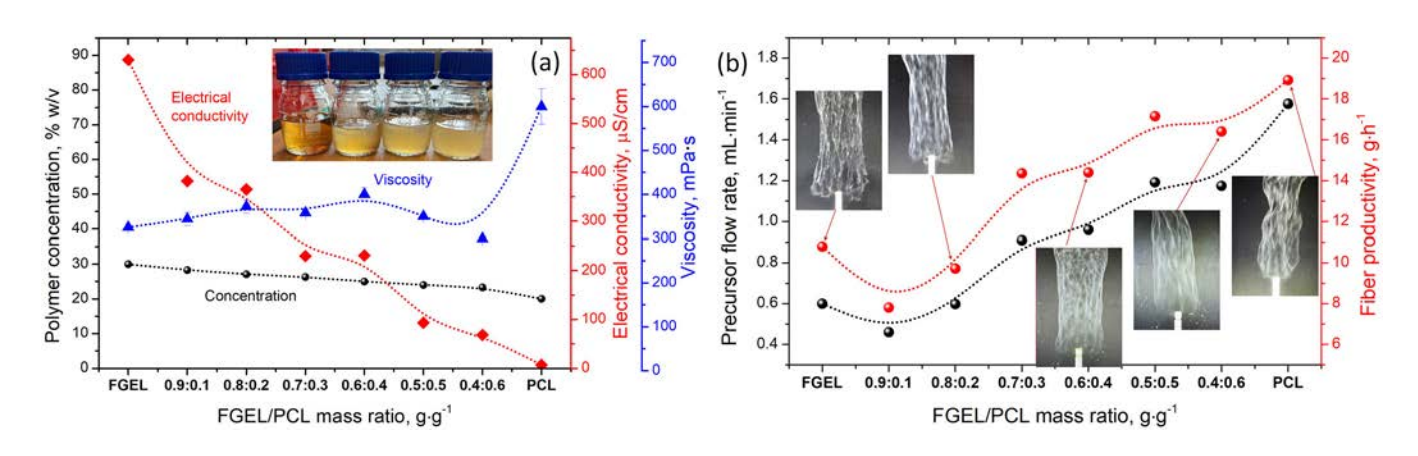


FIGURE 1 (a) Precursor concentration, viscosity, and electrical conductivity as a function of FGEL/PCL mass ratio with (inset) the appearance of pristine GEL (left) and FGEL/PCL precursors with the increasing content of PCL (from the left to the right); (b) Precursor flow take off rate and nanofiber productivity as a function of FGEL/PCL mass ratio. [Color figure can be viewed at wileyonlinelibrary.com]

result of partial agglomeration of PCL chains in the blended precursors. The blended precursors with the increasing PCL content reveal a gradual change from transparent to hazy appearance due to the formation of such small agglomerates of PCL (Figure 1a, inset). Furthermore, though the initial viscosity of pristine PCL precursor was substantially higher than the blended precursors, all of the PCL-containing precursors viscosities exhibited extreme sensitivity over time and declined steeply within a few days after preparation, resulting in decreased spinnability. Extended testing in ambient conditions of the viscosity over time of precursors containing higher concentrations of PCL were observed to decline in an exponential manner over 7 days. This steep decline in viscosity can be attributed to the ester hydrolysis of the PCL by the acidic solvent.<sup>24</sup> However, pristine gelatin precursor viscosity decreased minimally despite the acidic environment. It is also expected that the consequent physiochemical properties of the FGEL/PCL nanofibrous sheets may be affected by the partially hydrolyzed PCL component over time.<sup>25</sup> To better preserve the desired viscosity of the precursors containing PCL, they may be kept at lower temperatures to slow the hydrolytic effect and maintain higher PCL molar mass.

The NaAc salt additive and minute quantities of water in the FGEL/PCL precursors allowed for adjustment of the viscosity to fairly close values for all tested FGEL/PCL compositions and maintenance of the same precursor spinnability within the first 24–48 h of preparation. Prior study on AC-electrospinning of PCL indicated the need for NaAc<sup>14</sup> to create the shear-thinning effect in the viscosity behavior and improve PCL spinnability. In this respect, the presence of NaAc and water determined the observed changes in the electrical conductivity of all tested precursors (Figure 1a).

## 3.1.2 | Precursor spinnability, fibrous flow, and productivity

It was found that humidity above 30%, ambient temperature of 22°C, and 28–30 kV allowed for uniform and continuous spinning of all the precursor solutions. Propagating liquid jets were formed mainly along the edge of spinneret and some formed across the surface of the polymer

solution, creating a hollow cylindrical flow pattern. The fibrous flow is then carried upward toward the collector by the "electric wind" phenomena (Figure 1b).<sup>15</sup> A general trend of increased flow rate and productivity was observed with increased PCL content of the precursors (Figure 1b and Table 1). However, there was some variance seen in fiber mass collected for pristine PCL due to some inconsistency in the flow trajectory, causing a fraction of fibers to go astray. It was also noted that the fibrous flow is generally increasing in width with more PCL content in the precursor (Figure 2, inset). This can be related to the increased electric field in the precursor layer with lower electrical conductivity and thus larger electric force during the propagating jet formation that can broaden the generated fibrous flow.

#### 3.2 | Nanofibrous material analysis

## 3.2.1 | Textural properties of FGEL/PCL nanofibers

The collected FGEL and FGEL/PCL nanofibrous meshes were highly porous, with the porosity varying in the range 94%–96% (Figure 2). Close porosity values seem to be related to the small differences of the precursors' viscosity. The thermal cross-linking of as-spun FGEL/PCL nanofibrous meshes at 160°C for 4 h resulted in ~2% increase of porosity of FGEL/PCL materials with PCL mass content of 40 wt% and below. This can be due to the elimination of the residual solvent. Porosity of the FGEL/PCL materials with larger PCL content sharply reduces, mainly due to the partial melting of PCL component, nanofiber fusion and the mesh shrinkage.

SEM images show that FGEL and all FGEL/PCL nanofibers formed were beadless and smooth, with average diameters of 230–750 nm, depending on the FGEL/PCL ratio (Figure 3a–c and Table 2). A general trend of increased average fiber diameter with increased PCL content was observed. The change in fiber diameter for as-spun samples is largely the result of viscosity of the precursor solutions, although the effect of electrical conductivity cannot be ruled out. Thermal crosslinking results in the increase of fiber diameter in FGEL and 0.8:0.2 FGEL/PCL nanofibrous meshes, but the fiber

TABLE 1 Flow rates and fiber production rates for FGEL, FGEL/PCL, and PCL precursors with 25-mm diameter dish-like spinneret.

Parameters	FGEL	0.9:0.1	0.8:0.2	0.7:0.3	0.6:0.4	0.5:0.5	0.4:0.6	PCL
Flow rate [mL·min <sup>-1</sup> ]	0.6000	0.4620	0.5980	0.9100	0.9600	1.1920	1.1740	1.5748
Fiber production rate [g·h <sup>-1</sup> ]	10.800	7.8108	9.7235	14.359	14.400	17.165	16.413	18.922

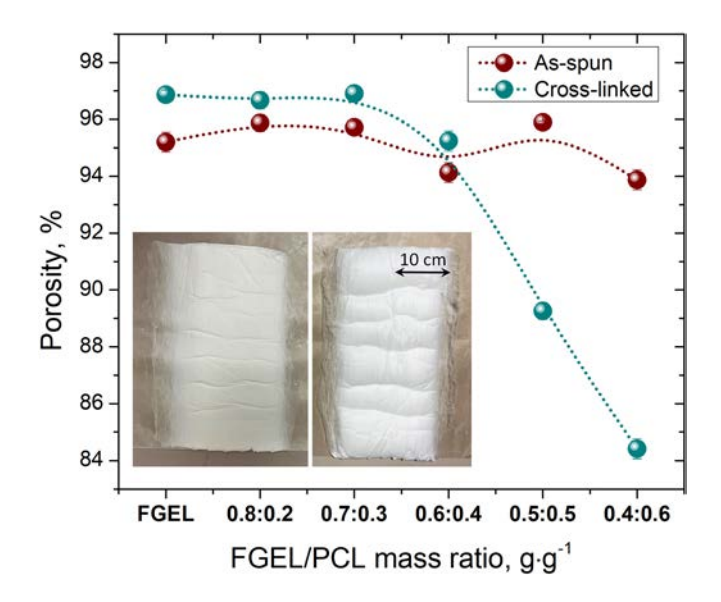


FIGURE 2 Porosity of as-spun and cross-linked nanofibrous sheets with different FGEL/PCL mass ratios with (inset) as-spun nanofibrous sheets with 0.6:0.4 (left) and 0.4:0.6 (right) FGEL/PCL mass ratios. [Color figure can be viewed at wileyonlinelibrary.com]

diameter decreases in nanofibrous meshes with higher PCL content (Table 2).

Crosslinked FGEL and FGEL/PCL nanofibers show no change in the appearance up to 0.6:0.4 FGEL/PCL mass ratio (Figure 3e-g). However, those with higher PCL content (i.e., 0.4:0.6 FGEL/PCL mass ratio, Figure 3h) clearly displayed melting of the PCL which decreased average fiber diameter and increased apparent fusing of the fibers into web-like structures (Figure 2h). Pristine PCL fibers displayed comparatively thin, beaded fibers with beading similar to those studied by Lawson. Pristine PCL nanofibers cannot be processed at the used temperatures due to complete melting, and they were therefore excluded from the analysis.

#### 3.2.2 | Structural analysis by FTIR and XRD

FTIR transmission spectra of the both as-spun and thermally cross-linked thin nanofibrous sheets with different FGEL/PCL mass ratios are shown in Figure 4.

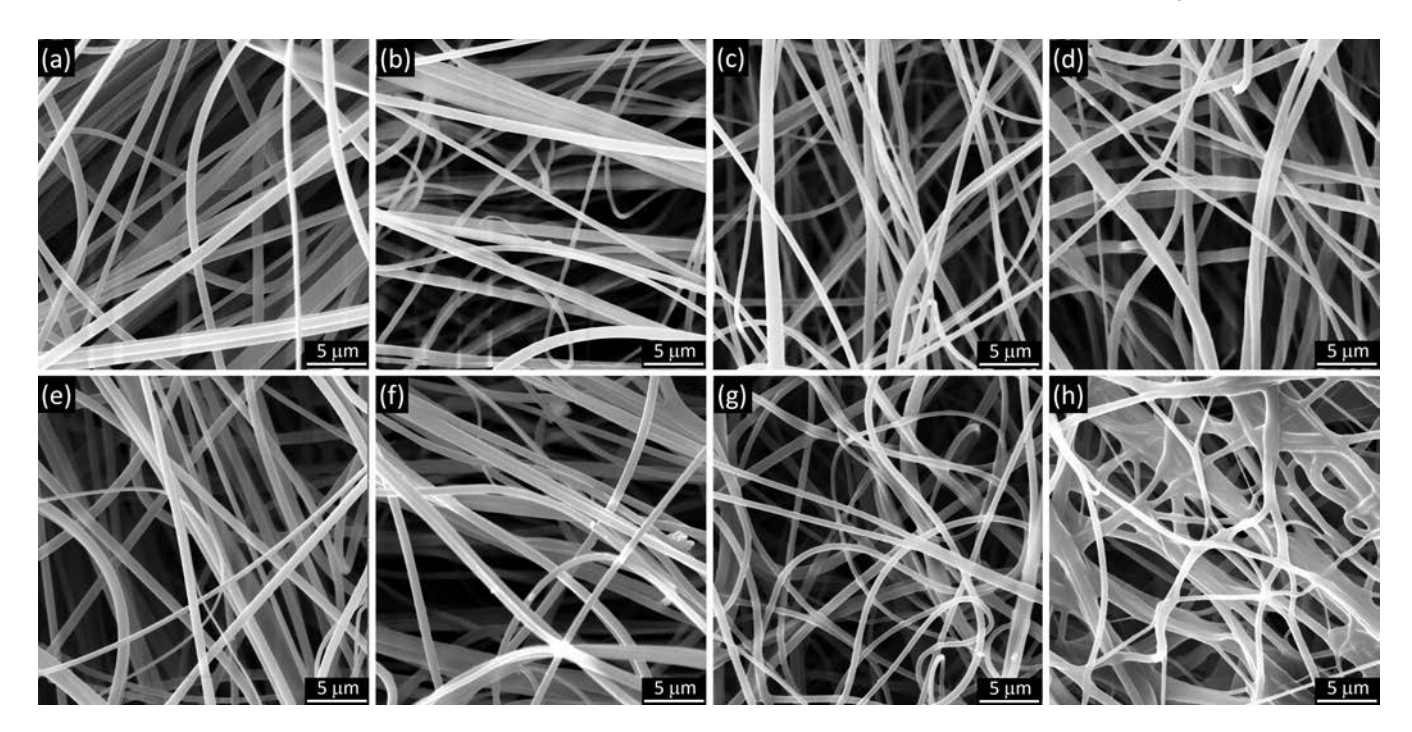


FIGURE 3 SEM images of (a-d) as-spun and (e-h) thermally cross-linked FGEL (a,e) and FGEL/PCL nanofibers with 0.8:0.2, 0.6:0.4 and 0.4:0.6 mass ratios, respectively.

TABLE 2 Average fiber diameters with standard deviations of as prepared and treated FGEL, FGEL/PCL, and PCL samples.

Parameter	Material	FGEL	0.9:0.1	0.8:0.2	0.7:0.3	0.6:0.4	0.5:0.5	0.4:0.6	PCL
As spun	Average diameter [nm]	534	237	612	620	645	605	741	268
	Std. Dev. [nm]	309	63	195	134	230	199	294	144
Cross-linked	Average diameter [nm]	694	-	634	597	595	587	596	-
	Std. Dev. [nm]	214	-	183	133	132	258	365	-

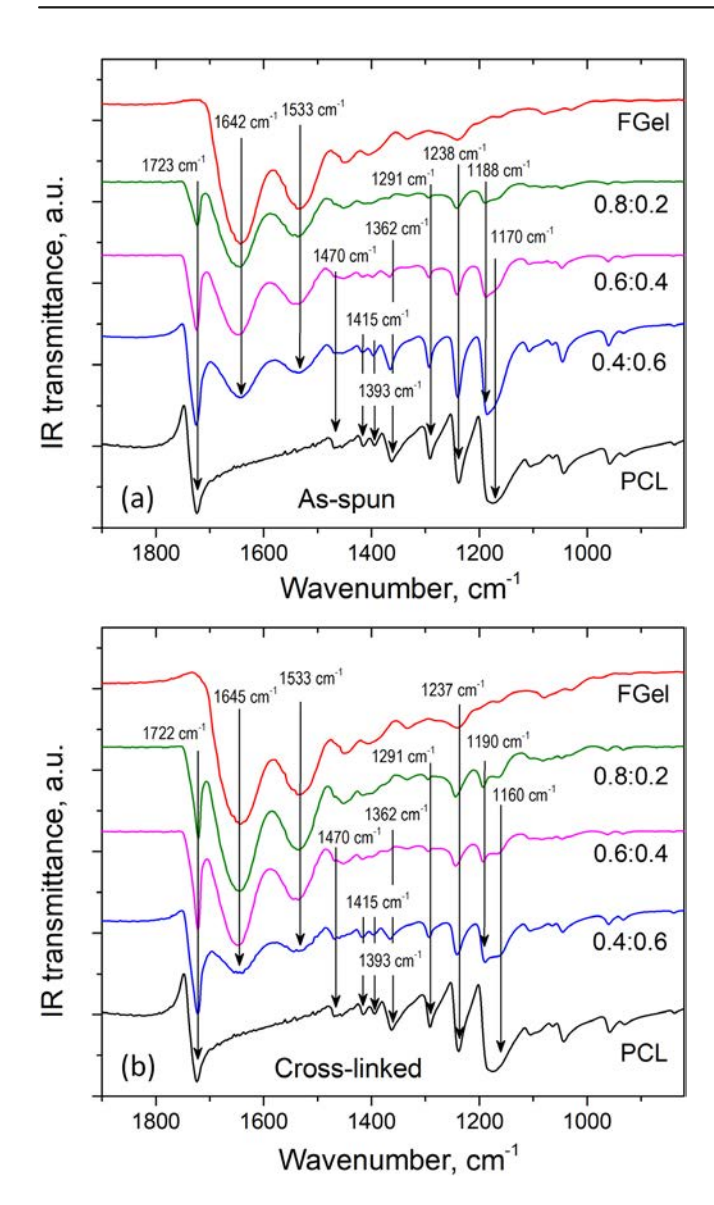


FIGURE 4 FTIR transmission spectra of (top) as-spun and (bottom) cross-linked nanofibrous sheets with different FGEL/PCL mass ratios. FTIR spectra of as-spun PCL nanofibers are shown for comparison in both graphs. [Color figure can be viewed at wileyonlinelibrary.com]

The characteristic peaks associated with IR absorption bands of PCL at  $1722 \, \mathrm{cm}^{-1}$  (C=O stretching),  $1362 \, \mathrm{cm}^{-1}$  (CH<sub>2</sub> wagging),  $1291 \, \mathrm{cm}^{-1}$  (C-C and C-O stretching in crystalline phase), and  $1238 \, \mathrm{cm}^{-1}$  (C-O-C asymmetric stretching in amorphous phase) show a slight shift to higher frequencies in FGEL/PCL nanofibers when compared to pristine PCL. The positions of the peaks at  $1470 \, \mathrm{cm}^{-1}$  (CH<sub>2</sub> scissoring),  $1415 \, \mathrm{cm}^{-1}$  (CH<sub>2</sub> bending), and  $1393 \, \mathrm{cm}^{-1}$  (CH<sub>2</sub> wagging) remain practically the same in as-spun FGEL/PCL nanofibers (Figure 5, top). The absorption band centered at  $\sim 1170 \, \mathrm{cm}^{-1}$  in pristine PCL nanofibers splits into two peaks at  $1188 \, \mathrm{cm}^{-1}$  (O-C-O stretching in crystalline

phase) and 1160 cm<sup>-1</sup> (C-O and C-C stretching in amorphous phase) in FGEL/PCL nanofibers. For the fish gelatin component of as-spun FGEL/PCL nanofibers, the most pronounced peaks at 1642 cm<sup>-1</sup> (Amide-I) and 1533 cm<sup>-1</sup> (Amide-II) slightly broaden toward the higher frequencies when compared to pristine FGEL nanofibers. Those frequency changes can indicate some degree of interaction between FGEL and PCL,<sup>28</sup> such as a possible hydrogen bond formation between ester group of PCL and amine group of FGEL,<sup>29</sup> or some level of the fibers' structural modification.

Thermal cross-linking of FGEL/PCL nanofibers resulted in the PCL band at  $1722 \text{ cm}^{-1}$  at the same position as in as-spun pristine PCL nanofibers and more noticeable split of  $1170 \text{ cm}^{-1}$  band into two peaks at  $1190 \text{ and } 1160 \text{ cm}^{-1}$ . The apparent position of FGEL Amide-I peak shifted to  $\sim 1645 \text{ cm}^{-1}$  in the cross-linked pristine FGEL and all FGEL/PCL samples (Figure 4, bottom).

The splitting of the absorption band observed at  $\sim$ 1170 cm<sup>-1</sup> in pristine PCL nanofibers into two peaks in FGEL/PCL nanofibers is associated with the changes in PCL crystallinity, where the bands at 1190 and 1160 cm<sup>-1</sup> are assigned to infrared light absorption in PCL crystalline and amorphous phases, respectively. A sharper peak at 1190 cm<sup>-1</sup> in cross-linked FGEL/PCL nanofibers can indicate a higher crystallinity of PCL fraction when compared to as-spun materials. It has also been observed that the intensity of PCL peaks in the range from 1400 to 1100 cm<sup>-1</sup> noticeably reduces with respect to the intensity of the peak at 1722 cm<sup>-1</sup> (Figure 4, bottom, and the example in Figure 5a). The latter band also displays some asymmetry due to the presence of a shoulder centered at  $\sim 1736 \text{ cm}^{-1}$ . This component is due to the amorphous phase in PCL, and the ratio of the peak intensities at 1722 and 1736 cm<sup>-1</sup> can be used to estimate the content of PCL crystalline and amorphous phases in nanofibers. The PCL crystallinity in AFES FGEL/PCL has been determined according to the procedure proposed by He and Inoue, 30 using the two Gaussian peaks curve fitting of the PCL absorption band centered at 1722 cm<sup>-1</sup>, as shown in the example in Figure 5b,c. The content of the crystalline phase was calculated using the expression

$$X_{\rm c} = I_{\rm c} \times 100\% / (I_{\rm c} + \gamma I_{\rm a}),$$
 (3)

where  $I_{\rm c}$  and  $I_{\rm a}$  are the intensities of the 1722 and 1736 cm<sup>-1</sup> peaks, respectively, and the absorption coefficient  $\gamma$  is equal to 1.46  $\pm$  0.03. The calculation using this procedure revealed 69.2% crystallinity in AFES pristine PCL nanofibers, and 69.5% crystallinity in the precursor bulk PCL.

This crystallinity parameter is higher than 54%–58% crystallinity determined from either FTIR or differential scanning calorimetry (DSC) data of AFES pristine PCL fibers from several formic acid-based precursors, <sup>31</sup> or 42%–56% and 35%–38% crystallinity determined by DSC<sup>32</sup> and XRD, <sup>33</sup> respectively, for DC electrospun PCL nanofibers from an acetic acid precursor. <sup>32</sup> According to the results displayed in Table 3 the crystallinity of PCL initially increases but then reduces significantly with the increasing content of FGEL in as-spun FGEL/PCL nanofibers, when compared to as-spun pristine PCL. This partially agrees with the results for PCL/Gelatin

nanofibers,<sup>34</sup> where it was suggested that gelatin can inhibit the PCL crystallization. The crystallinity of PCL component increases in all FGEL/PCL compositions after the thermal cross-linking of nanofibers (Table 3), similarly to the example in Figure 5b,c for the AFES nanofibrous sample with 0.6:0.4 FGEL/PCL mass ratio.

More detailed analysis of the PCL absorption bands in the range from 1400 to 1100 cm $^{-1}$  in as-spun nanofibers with different FGEL/PCL mass ratios reveals the reduced peak intensities at 1238 and 1291 cm $^{-1}$  with respect to the intensity of the peaks at 1722, 1470, and 1415 cm $^{-1}$ . The intensity ratios  $I_{1291}/I_{1722}$  and  $I_{1238}/I_{1722}$ 

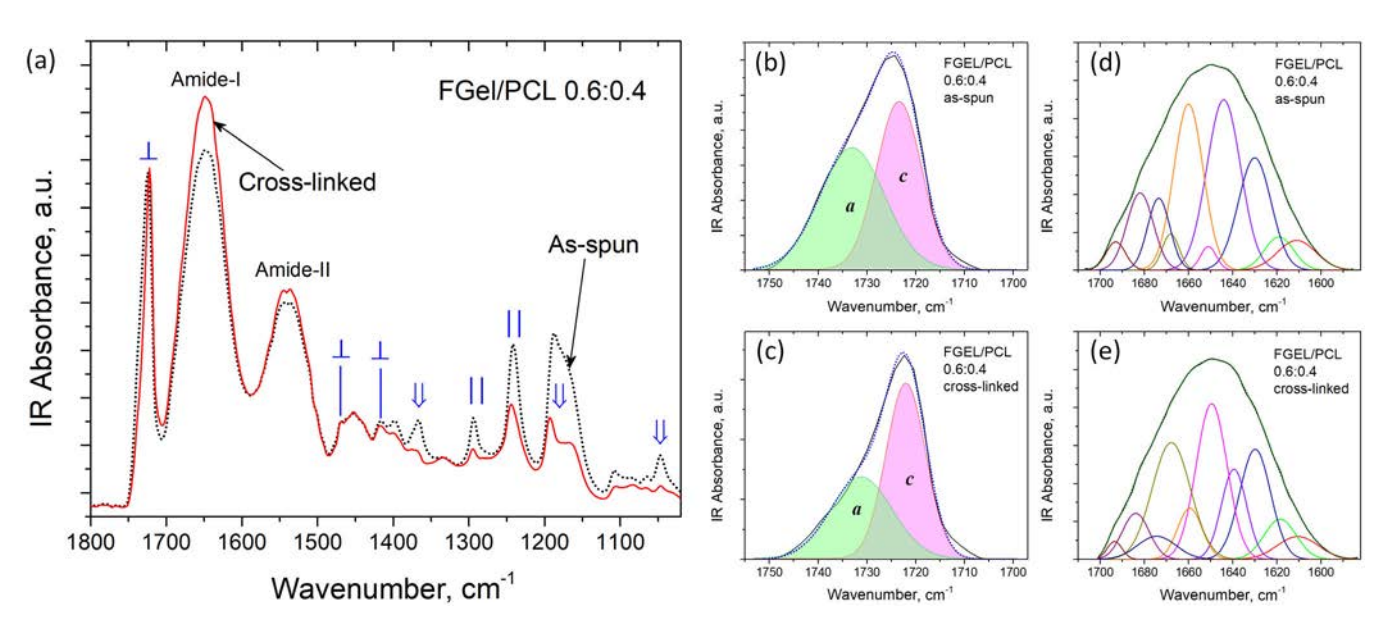


FIGURE 5 (a) Representative FTIR absorption spectra, (b,c) Curve fittings of 1722 cm<sup>-1</sup> absorption band, and (c) Amide-I absorption band curve fitting based on 2nd derivative spectrum of as-spun and cross-linked FGEL/PCL nanofibers with 0.6:0.4 polymer mass ratio. [Color figure can be viewed at wileyonlinelibrary.com]

TABLE 3 Structural parameters of as-spun and thermally crosslinked (denoted as \*) FGEL/PCL nanofibers derived from FTIR spectra.

			Fish gelatin secondary structure (% fraction or ratio)					XRD		
Material	PCL crystallinity, FTIR [%]	Ratio $I_{1237}/I_{1722}$ and $I_{1295}/I_{1722}$	α-Helix	Coil	β-Sheet + β-turn	Helix/ coil ratio	Helix/ sheet ratio	Sheet/ coil ratio	PCL crystallinity [%]	Crystalline domain size [nm]
FGEL	-	-	21.1	19.6	59.3	1.08	0.36	3.03	-	-
0.8:0.2	40.2	0.44/0.16	24.2	24	51.8	1.01	0.47	2.16	n/d	n/d
0.6:0.4	48.7	0.47/0.19	25.4	28.3	46.3	0.9	0.55	1.63	40.3	26.4
0.4:0.6	80.8	0.61/0.37	28	26.6	45.5	1.05	0.62	1.71	67.7	29.4
FGEL*	-	-	20.8	21.1	58	0.99	0.36	2.74	-	-
0.8:0.2*	48.4	0.26/0.10	22.7	27.4	49.9	0.83	0.46	1.82	n/d	n/d
0.6:0.4*	52	0.29/0.11	27.6	34	38.4	0.81	0.72	1.13	47.3	40.6
0.4:0.6*	88	0.34/0.23	15	33.9	51.1	0.44	0.3	1.51	76.4	40.8
PCL	69.2	0.62/0.41	-	-	-	-	-	-	52.0	34.7

are presented in Table 3. Those intensity ratios gradually decrease with the increasing FGEL/PCL mass ratio in asspun nanofibers, and then proportionally decrease considerably more after the fibers are thermally cross-linked, as shown in the exemplary FTIR spectra in Figure 5a.

The peaks at 1238 and 1291 cm<sup>-1</sup> are associated with the vibrational modes, which are parallel to the PCL polymer chain. It should be noted that these peaks shift to 1243 and 1295 cm<sup>-1</sup>, respectively, in cross-linked FGEL/PCL nanofibers. This is related to the increase in crystallinity of PCL component.<sup>35,36</sup> Other three peaks  $(1722, 1470, and 1415 cm^{-1})$  are due to the vibrational modes perpendicular to the main chain direction.<sup>27,37</sup> The reduction in the intensity of absorption bands associated with the vibrational modes parallel to PCL main chain direction has been observed when the incident infrared light was polarized perpendicular to the fiber axis. 32,38 The intensity of the band centered at 1170 cm<sup>-1</sup> also reduces, although the change in the intensity of its components at 1192 and 1160 cm<sup>-1</sup> in AFES FGEL/PCL nanofibers show the opposite trends when compared to those observed by Xu.<sup>37</sup> Although the FTIR analysis in present work was performed in transmission mode by using unpolarized infrared light, the nanofibrous sheets were always oriented perpendicular to infrared beam direction. Therefore, the reason for the intensity changes of the discussed infrared absorption bands can be the alignment of c-axis of PCL crystalline domains in the direction perpendicular to the fiber axis, instead of its initial orientation mostly along the stretching direction of fibers in the propagating fibrous flow. The degree of such alignment is relatively small in as-spun FGEL/PCL nanofibers, although it increases at higher FGEL/PCL mass ratios, likely due the changes in crystallization kinetics of PCL in radially restricted volume of a drying, mostly FGEL nanofiber in a slowly moving fibrous flow in AFES at room temperature. 39,40 However, during the thermal cross-linking the PCL phase melts and re-crystallize under the physical confinement of PCL crystalline domains and chain agglomerates between the amorphous segments of FGEL. This can cause the observed alignment of PCL crystalline domains in the cross-linked material.41

The analysis of another part of FTIR spectra of FGEL/PCL nanofibers, namely Amide-I absorption band, provides the insights into the secondary fish gelatin structure in the as-spun and cross-linked materials. The Amide-I bands were deconvoluted into ten overlapping component bands by using the peak positions determined for its second derivative spectrum (Figure 5d,e). The component band assignments to  $\alpha$ -helices (1660 and 1668 cm<sup>-1</sup>),  $\beta$ -sheets (1611, 1619, 1630, and 1693 cm<sup>-1</sup>),  $\beta$ -turns (1673 and 1682 cm<sup>-1</sup>), and random coil (1644

and 1650 cm<sup>-1</sup>) structures were made based on the data from various sources, <sup>42-46</sup> especially those on Amide-I band of fish gelatin. <sup>47-49</sup>

The results of curve fitting are shown in Table 3 and reveal several apparent trends. First, both α-helix/random coil and β-sheet/coil ratios in as-spun FGEL and FGEL/PCL nanofibers gradually decrease, whereas α-helix/β-sheet ratio increases with the increasing amount of PCL in the material. However, these trends occur mainly because of substantial reduction in the content of  $\beta$ -sheets and  $\beta$ -turns combined, while the relative content of both helix and coil structures actually increases with the increasing amount of PCL. Second, thermal crosslinking of pristine FGEL nanofibers only slightly reduces the content of both  $\alpha$ -helix and  $\beta$ -sheet structures. Third, the α-helix/random coil ratio in thermally cross-linked FGEL and FGEL/PCL nanofibers decrease further at a higher rate with the increasing amount of PCL in the material. However, there were no other clear trends established for the crosslinked nanofibers. Interestingly, the crosslinked material with 0.6:0.4 FGEL/PCL mass ratio exhibited apparently the highest  $\alpha$ -helix/ $\beta$ -sheet ratio, lowest  $\beta$ -sheet/coil ratio, and the lowest content of  $\beta$ -sheets and  $\beta$ -turns combined. Also, a much lower content of α-helices was found in nanofibers with 0.4:0.6 FGEL/PCL mass ratio, when compared to other compositions.

X-ray diffraction patterns of AFES FGEL, PCL, and FGEL/PCL nanofibers are shown in Figure 6a,b.

The peak positions at 16.1, 21.35, 21.9 and 23.6°  $2\theta$ were assigned to (102), (110), (111) and (200) plane reflections in the PCL crystalline domains, and FGEL fraction was amorphous. The PCL crystallinity and crystalline domain sizes determined from the curve fitting with Voigt function as shown in the representative patterns in Figure 6c,d, is presented in Table 3. Although it was not possible to determine the crystallinity in nanofibers with 0.8:0.2 FGEL/PCL mass ratio due to the low diffraction peaks intensity, the trends in crystallinity were generally the same as those obtained from FTIR data, although the calculated crystallinity values from XRD data were proportionally lower. The average size of PCL crystalline domains in pristine PCL nanofibers was calculated as 34.7 nm. This is noticeably larger than the 16.5–19.2 nm size of PCL crystalline domains in AFES PCL nanofibers prepared from formic acid-based precursors, although the crystallinity was similar. On the contrary, Ferreira et al<sup>33</sup> reported a closer, 25.3–28.7 nm size of crystalline domains at much lower crystallinity (35.3%-37.7%) in PCL nanofibers that were DC electrospun from the acetic acid precursor. It can be concluded that both the process and precursor parameters play a role in the resulting structure of PCL nanofibers. The average crystalline

10974628, 0, Downloaded from https://onlinelibrary.wiley.com/doi/10.1002/app.54376, Wiley Online Library on [03/07/2023]. See the Terms and Conditions (https://onlinelibrary.wiley.com/terms-and-conditions) on Wiley Online Library for rules of use; OA articles are governed by the applicable Cenative Commons License

domain size of PCL fraction was found to decrease with the increasing content of FGEL in FGEL/PCL nanofibers (Table 3). However, the thermal cross-linking increases the size of crystalline domains due to the melting and recrystallization of PCL fraction. This correlates with the increasing crystallinity of crosslinked FGEL/PCL nanofibers.

#### 3.2.3 | Wettability characterization

Surface wettability is one of the important parameters that influences the cell/substrate interaction<sup>50</sup> although the relationship between the wettability and cell behavior is not straightforward.<sup>51,52</sup> The wettability of nanofibrous

substrates can differ significantly from the other forms of the same material, such as thin films or bulk. For example, a nanofibrous layer of a partially wettable material can behave like a superhydrophobic substrate when a droplet of fluid is gently placed on its surface.<sup>53</sup>

The images of a 2 mm diameter water droplet behavior on the surface of AFES FGEL/PCL nanofibrous substrates and the measured contact angles are shown in Figure 7. It can be seen that the WCA, measured after the droplet was placed and stabilized for 0.1 s, was larger than 90° for all samples (Figure 7b). The largest WCAs (112° and 117°) were observed for FGEL/PCL nanofibrous substrates with 0.8:0.2 and 0.7:0.3 polymer mass ratios, respectively. The droplet absorption also varied notably between the samples with different compositions

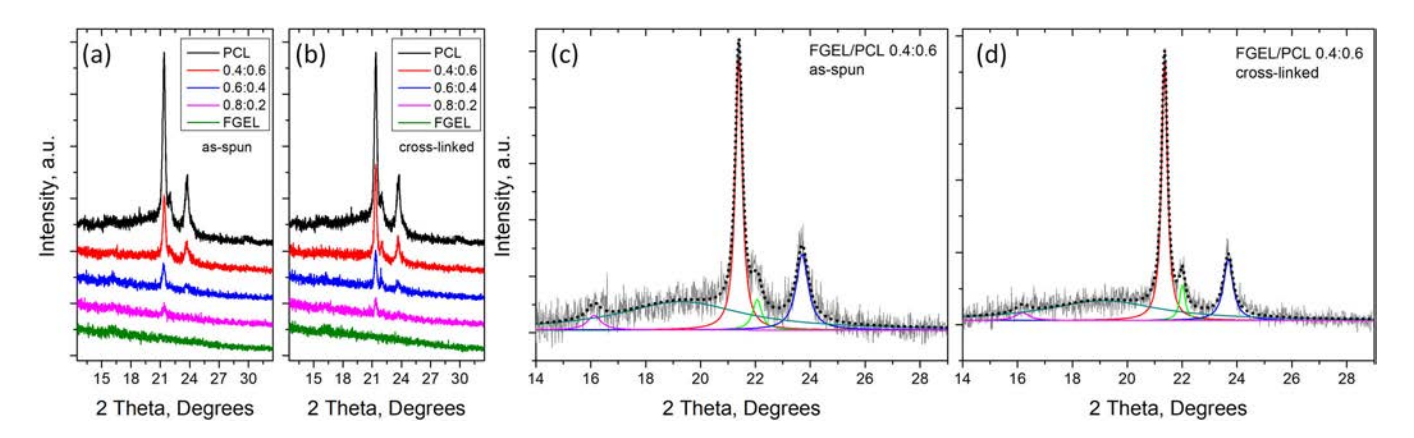


FIGURE 6 XRD patterns of (a) as-spun and (b) thermally cross-linked AFES FGEL, PCL, and FGEL/PCL nanofibers; Representative curve fittings of (c) as-spun and (d) cross-linked FGEL/PCL nanofibers with 0.6:0.4 polymer mass ratio. [Color figure can be viewed at wileyonlinelibrary.com]

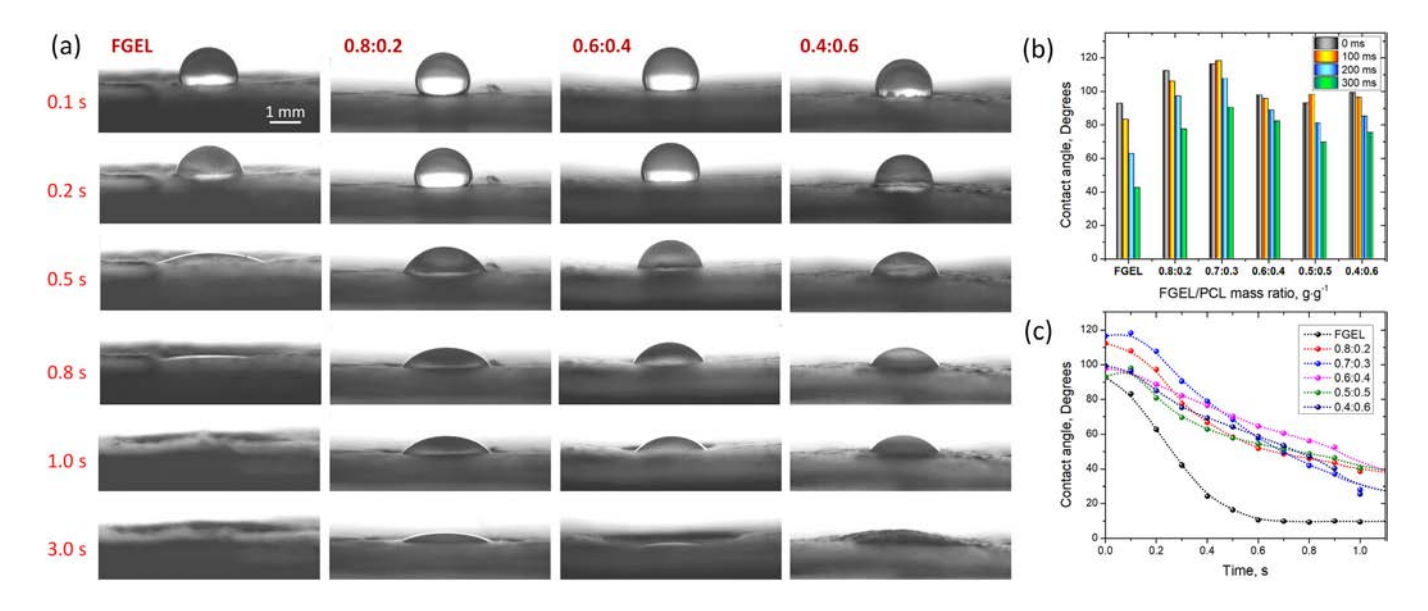


FIGURE 7 (a-c) Temporal changes in the water contact angle of FGEL and FGEL/PCL nanofibrous sheets with different composition. [Color figure can be viewed at wileyonlinelibrary.com]

(Figure 7a). The WCA reduced quickly from  $93^{\circ}$  to  $40^{\circ}$  (at 0.3 s) and then below  $20^{\circ}$  (at 0.5 s) for a pristine FGEL nanofibrous substrate. For all FGEL/PCL samples the WCA reduction was more gradual and ranged within  $117-93^{\circ}$  at 0.1 s,  $70-58^{\circ}$  at 0.5 s, and then within  $40.6-25.5^{\circ}$  at 1.0 s (Figure 7c).

Jalili et al<sup>54</sup> reported the WCAs in the range from 18° to 76° for pristine gelatin nanofibers (80-140 nm diameter) prepared by DC electrospinning at different voltages and distances. It was noted that the WCA was lower for a larger pore size (up to 15 mm) and smaller surface area (down to 5  $\text{m}^2 \cdot \text{g}^{-1}$ ) of the material. On the other hand, WCA of 116° was reported for pristine gelatin films<sup>55</sup> and ascribed to the dominance of nonpolar chains of protein molecules at the film surface after the evaporation of solvent. WCA values for the electrospun pristine PCL nanofibers were reported between 84° and 136°, and they were strongly affected by the solvent and process parameters, 56-58 whereas PCL films exhibited smaller (50–80°) WCAs. <sup>20,59</sup> It was proposed that the wettability of electrospun PCL nanofibrous substrates is affected mainly by the surface roughness, porosity and fiber packing.20

The WCA of PCL and gelatin partially blended nanofibers has been reported between 20° and 108° 60-62 and it depended on the gelatin-to-PCL mass ratio, among the other factors. For example, DC-electrospun gelatin/PCL blends with 0.8:0.2 mass ratio revealed 106° WCA, 62 which is close to WCA of 112° for AFES FGEL/PCL nanofibrous substrate with the same mass ratio within 0.2 s time interval of the droplet placement. Another report shows that the WCA of DC electrospun 0.5:0.5 gelatin/PCL nanofibers reduce from  $\sim$ 58° to 20° after 5 s the droplet was placed and to 0° after 10 s exposure. It would take less than 3 s for the droplet to absorb entirely on AFES FGEL/PCL nanofibrous substrate with similar composition (Figure 7). On the other hand, Hu et al<sup>60</sup> noted only moderate reduction of WCA from 62° to 50° during 20 s in their DC electrospun 0.7:0.3 gelatin/PCL nanofibrous membranes, whereas the 0.7:0.3 AFES FGEL/PCL nanofibrous material showed the WCA reduction from 116° to 28° within 1 s time interval.

It has been proposed that the high WCA and water droplet behavior on AFES FGEL/PCL thermally cross-linked nanofibrous substrates are affected by their very high porosity (~96%), changes in wettability of blended fibers, and layered nanofibrous sheet structure, in particular at higher FGEL/PCL mass ratios. This determines the degree of competition between the lateral and vertical components of fluid transport through the nanofibrous substrate. It appears that the lateral components decrease with respect to vertical component with the increased content of PCL. This is the most visible for 0.6:0.4 FGEL/

PCL sample, where the droplet appears to sink into the substrate while its diameter shows the least increase. However, at lower FGEL/PCL ratios the increased fusion between the fibers due to PCL melting and recrystallization plays an increasing role, and the situation is reversed. Specifically for 0.4:0.6 FGEL/PCL material, the fiber fusion and decreased porosity could have led to more lateral water diffusion and swelling of the topmost layer (Figure 7a). The droplet seems to be primarily in Cassie-Baxter state<sup>63,64</sup> for all tested compositions, although for FGEL/PCL mass ratios lower than 0.5:0.5 there may be a contribution of Wenzel state<sup>65</sup> due to significant morphological changes of the nanofibrous substrate.

#### 3.3 | Initial cellular response analysis

Cellular response as indicated by representative SEM images was promising, showing good cellular attachment, spreading, proliferation, and eventual confluence for several samples. Initial cell attachment was present for all samples day 1, with continued attachment and spreading through day 7, as seen in representative images of FGEL/PCL with 0.8:0.2, 0.6:0.4, and 0.4:0.6 mass ratios (Figure 8).

Cells elongated along the fibrous structures and formed spindle shaped morphology with textured surfaces consistent with viability. 66,67 Attached cells proliferated and neared confluence for more FGEL-rich samples by day 7, while those with higher PCL content neared confluence by day 14. Spreading cells continued along fibers and remained textured while forming fibril-like connections between viable cells by day 3, indicating intercellular communication, good health, and increased structural integrity.66 These properties were increased as cells proliferated toward confluence. However, PCL-dominant samples tended to have smoother cell textures compared to those on FGEL-dominant samples as cell clusters formed. The FGEL-rich samples with up to 0.6:0.4 FGEL/PCL mass ratio allowed for a confluent monolayer of cells at day 14. The samples with higher PCL content did not form a fully confluent monolayer but had minimal gaps visible between groups of cells (sample 0.4:06 after 7 days in Figure 8). This behavior can be attributed to the morphological and porosity changes in this sample after the crosslinking. Such changes can lead to weaker attachment of cells to the meshes, slower attachment, and/or spreading due to attachment difficulty.<sup>68</sup> The factor of reduced porosity is also the cause of cells' tendency to remain on the surface of the meshes to form a layer, as opposed to penetrating the mesh.<sup>66,68</sup> Additionally, Gomes et al<sup>68</sup> note that more

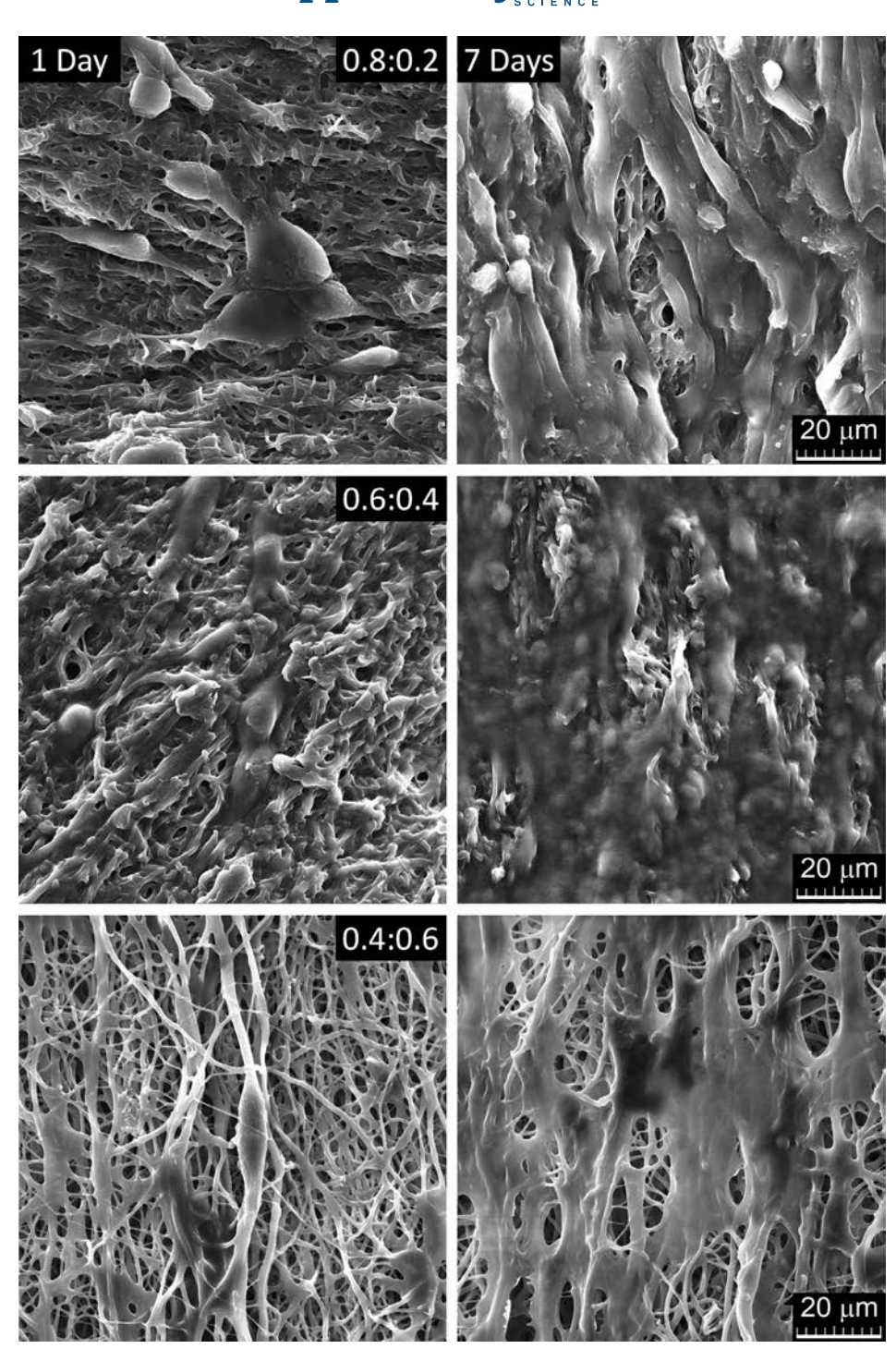
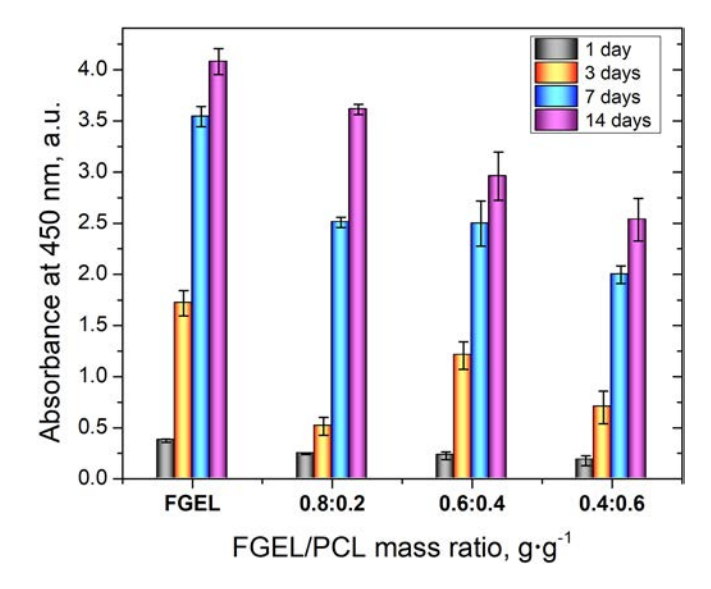


FIGURE 8 SEM images of 3 T3 mouse fibroblast cells grown for 1 and 7 days on nanofibrous substrates with FGEL/PCL mass ratios of 0.8:0.2, 0.6:0.4 and 0.4:0.6.

time in culture may be necessary for the cells to begin digestion of the meshes such that they can penetrate the surface, or perhaps the introduction of an external signaling factor to promote the behavior. Overall, during the 7-day time period, a trend of increased cellular attachment/spreading and proliferation was observed with increased FGEL content of the meshes. SEM revealed further that the fibrous structure of the blended FGEL/PCL meshes is retained for the entire duration of the cellular studies regardless of sample composition (Figure 8).

CCK-8 metabolic assays supported trends seen in SEM images. After 1 day cells were metabolically active for all samples with continued upward trend at days 3, 7, and 14 (Figure 9). However, activity of all samples suggested near confluence or confluence at days 7 and 14, dependent on sample composition. Overall, the observed trends in Figure 8 and 9 indicate that nutritionally supplemental nature of FGEL supports this behavior of cells. This also explains the continuing increase in absorbance of pristine FGEL on day 14, although the



**FIGURE 9** Absorption values of CCK-8 metabolic assay of cell cultures with FGEL and selected FGEL/PCL nanofibrous material after 1, 3, 7, and 14 days. [Color figure can be viewed at wileyonlinelibrary.com]

FGEL nanofibrous mesh was completely dissolved after 7 days.

The standard deviation values for absorbance data in Figure 9 varied from 0.006 to 0.237 depending on the material and test period. A basic one-way statistical ANOVA analysis of variance (alpha values <0.05, p values  $\le$ 0.001) indicated that the mean absorbance values of all samples at all cell metabolic activity test periods were statistically significant.

#### 4 | CONCLUSIONS

High productivity (7.8–19 g⋅h<sup>-1</sup>) of FGEL/PCL nanofibrous materials has been achieved with a "green" alternating field electrospinning process. The diverse range of compositions used (0.9:0.1–0.4:0.6 FGEL/PCL mass ratio) resulted in spinnable precursors despite their varying immiscibility, viscosities, and electrical conductivities. The formed nanofibrous materials exhibited an equally diverse range of microarchitectural and structural characteristics. FTIR and XRD exposed the importance and influence of composition and post-fabrication treatment of the materials with respect to the interaction of PCL and FGEL, crystallinity and orientation of PCL domains, and secondary structures of FGEL such that alteration of the composition leads to distinct differences in the nanofibrous material properties. SEM imaging, water contact angle, and porosity analysis revealed the morphological effects imparted by post-fabrication thermal treatment, especially on PCL-rich samples.

Additionally, preliminary test results of cellular viability with the blended FGEL/PCL nanofibers indicate promising use of such materials for various biomedical applications. This sustainable, noncytotoxic material could mean improved solutions for some of the medical field's most interesting problems within skin therapy, tissue engineering, or wound healing with low environmental impact at an affordable cost.

Overarchingly, confirmation of AFES as a viable highthroughput method for the formation of compositionally diverse gelatin/PCL nanofibrous materials can provide a pathway for a scalable, sustainable, and cost-efficient production of tailorable, biologically relevant materials.

Despite the thorough analysis conducted, more studies will be needed for clarification and expansion of the material performances for intended applications. Complementary to this, further optimization of the solvent system is foreseen to improve the miscibility of FGEL and PCL and to accommodate various additives. Finally, comprehensive mechanical, degradation, and cellular interaction evaluation in future studies could allow comprehensive assessment of the materials' biomedical potential.

#### **AUTHOR CONTRIBUTIONS**

Hannah A. Lacy: Conceptualization (lead); investigation (lead); writing – original draft (lead). Věra Jenčová: Methodology (equal); supervision (supporting). Šarká Hauzerová: Investigation (equal). Andrei Stanishevsky: Formal analysis (equal); visualization (equal); writing – review and editing (equal).

#### **ACKNOWLEDGMENTS**

This work was supported by the U.S. Department of Education GAANN Program [grant number P200A180001] and by the National Science Foundation (NSF) International Research Experience for Students (IRES) award to UAB [Grant Number 1852207]. The authors would like to thank Dr. David Lukáš and Dr. Tomas Kalous for the valuable technical assistance.

#### CONFLICT OF INTEREST STATEMENT

The authors declare that they have no known competing financial interests or personal relationships that could have appeared to influence the work reported in this paper.

#### DATA AVAILABILITY STATEMENT

Data is available from the Wiley Online Library or from the author.

#### ORCID

Andrei Stanishevsky https://orcid.org/0000-0002-8148-534X

## 14 of 15 | WILEY\_Applied Polymer

#### REFERENCES

- [1] C. T. Lim, Prog. Polym. Sci. 2017, 70, 1.
- [2] A. Eatemadi, H. Daraee, N. Zarghami, H. Melat Yar, A. Akbarzadeh, Artif. Cells Nanomed. Biotechnol. 2016, 44, 111.
- [3] J. Cui, F. Li, Y. Wang, Q. Zhang, W. Ma, C. Huang, Sep. Purif. Technol. 2020, 250, 117116.
- [4] S. Jiang, Y. Chen, G. Duan, C. Mei, A. Greiner, S. Agarwal, Polym. Chem. 2018, 9, 2685.
- [5] S. K. Ghosh, P. Adhikary, S. Jana, A. Biswas, V. Sencadas, S. D. Gupta, B. Tudu, D. Mandal, *Nano Energy* 2017, 36, 166.
- [6] K. Ghosal, A. Manakhov, L. Zajíčková, S. Thomas, AAPS PharmSciTech 2017, 18, 72.
- [7] V. Perez-Puyana, P. Wieringa, Y. Yuste, F. de la Portilla, A. Guererro, A. Romero, L. Moroni, J. Biomed. Mater. Res. A 2021, 109, 1600.
- [8] S. Gomes, G. Rodrigues, G. Martins, C. Henriques, J. C. Silva, Int. J. Biol. Macromol. 2017, 102, 1174.
- [9] Z. Wang, H. Wang, J. Xiong, J. Li, X. Miao, X. Lan, X. Liu, W. Wang, N. Cai, Y. Tang, *Mater. Sci. Eng. C* 2021, 128, 112287.
- [10] P. Pokorny, E. Kostakova, F. Sanetmik, P. Mikes, J. Chvojka, T. Kalous, M. Bilek, K. Pejchar, J. Valtera, D. Lukáš, *Phys. Chem. Chem. Phys.* 2014, 16, 26816.
- [11] J. Valtera, T. Kalous, P. Pokorny, O. Batka, M. Bilek, J. Chvojka, P. Mikes, E. Kuzelova Kostakova, J. Spankova, J. Beran, A. Stanishevsky, D. Lukáš, *Sci. Rep.* 2019, 9, 1801.
- [12] S. L. Nealy, C. Severino, W. A. Brayer, A. Stanishevsky, RSC Adv. 2020, 10, 6840.
- [13] P. Holec, R. Jirkovec, T. Kalous, O. Bat'ka, J. Brožek, J. Chvojka, *Nanomater.* **2022**, *12*, 665.
- [14] C. Lawson, A. Stanishevsky, M. Sivan, P. Pokorny, D. Lukáš, J. Appl. Polym. Sci. 2015, 133, 43232.
- [15] M. Sivan, D. Madheswaran, S. Hauzerova, V. Novotny, V. Hedvicakova, V. Jencova, E. K. Kostakova, M. Schindler, D. Lukáš, *Mater. Today Chem.* 2022, 26, 101025.
- [16] R. Jirkovec, T. Kalous, J. Chvojka, Mater. Des. 2021, 210, 110096.
- [17] R. Jirkovec, J. Erben, P. Sajdl, J. Chaloupek, J. Chvojka, *Mater. Des.* 2021, 205, 109748.
- [18] R. Jirkovec, T. Kalous, W. A. Brayer, A. V. Stanishevsky, J. Chvojka, Mater. Lett. 2019, 252, 186.
- [19] A. Kennell, M. MacEwen, M. Armstrong, T. Nicola, B. Halloran, N. Ambalavanan, A. Stanishevsky, *Mater. Today Comm.* 2022, 31, 103417.
- [20] P. K. Szewczyk, D. P. Ura, S. Metwally, J. Knapczyk-Korczak, M. Gajek, M. M. Marzec, A. Bernasik, U. Stachewicz, *Polymer* 2019, 11, 34.
- [21] Y. Zhang, H. Ouyang, C. T. Lim, S. Ramakrishna, Z. M. Huang, J. Biomed, *Mater. Res. B Appl.* **2005**, *72*, 156.
- [22] L. Daelemans, I. Steyaert, E. Schoolaert, C. Goudenhooft, H. Rahier, K. De Clerck, *Nanomaterials* **2018**, *8*, 551.
- [23] A. Stanishevsky, R. Yager, J. Tomaszewska, M. Binczarski, W. Maniukiewicz, I. Witońska, D. Lukáš, Ceram. Int. 2019, 45, 18672.
- [24] M. Bartnikowski, T. R. Dargaville, S. Ivanovski, D. W. Hutmacher, *Prog. Polym. Sci.* **2019**, *96*, 1.
- [25] O. Gil-Castell, J. D. Badia, A. Ribes-Greus, Eur. Polym. J. 2018, 101, 273.
- [26] M. J. Motiwalla, P. P. Punyarthi, M. K. Mehta, J. S. D'Souza, V. Kelkar-Mane, J. Environ. Biol. 2013, 34, 43.

- [27] T. Elzein, M. Nasser-Eddine, C. Delaite, S. Bistac, P. Dumas, J. Colloid Interface Sci. 2004, 273, 381.
- [28] M. Bikuna-Izagirre, J. Aldazabal, J. Paredes, Polymers 2022, 14, 1311.
- [29] Â. Semitela, A. F. Girão, C. Fernandes, G. Ramalho, I. Bdikin, A. Completo, P. A. A. P. Marques, J. Biomater. Appl. 2020, 35, 471.
- [30] Y. He, Y. Inoue, Polym. Int. 2000, 49, 623.
- [31] M. Sivan, D. Madheswaran, M. Asadian, P. Cools, M. Thukkaram, P. van der Voort, R. Morent, N. de Geyter, D. Lukáš, Surf. Coat. Technol. 2020, 399, 126203.
- [32] S. Ramazani, M. Karimi, E-Polymers 2014, 14, 323.
- [33] J. L. Ferreira, S. Gomes, C. Henriques, J. P. Borges, J. C. Silva, J. Appl. Polym. Sci. 2014, 131, 41068.
- [34] G. Prado-Prone, M. Bazzar, M. L. Focarete, J. A. García-Macedo, J. Perez-Orive, C. Ibarra, C. Velasquillo, P. Silva-Bermudez, *Biomed. Mater.* 2020, 15, 035001.
- [35] K. Phillipson, J. N. Hay, M. J. Jenkins, *Thermochim. Acta* 2014, 595, 74.
- [36] D. Rohindra, R. Lata, K. Kuboyama, T. Ougizawa, *Polym. Cryst.* 2019, 2, 10037.
- [37] S. Xu, J. Rowlette, Y. J. Lee, Opt. Express 2022, 30, 8436.
- [38] X. Wang, H. Zhao, L. S. Turng, Q. Li, Ind. Eng. Chem. Res. 2013, 52, 4939.
- [39] T. Sakurai, H. Nagakura, S. Gondo, S. Nojima, *Polym. J.* 2012, 45, 436.
- [40] R. Wan, X. Sun, Z. Ren, H. Li, S. Yan, Materials 2020, 13, 5655.
- [41] R.-M. Ho, Y.-W. Chiang, C.-C. Lin, B.-H. Huang, R.-M. Ho, Macromolecules 2005, 38, 4769.
- [42] J. Kong, S. Yu, Biochim. Biophys. Sin. 2007, 39, 549.
- [43] X. Hu, D. Kaplan, P. Cebe, Macromolecules 2006, 39, 6161.
- [44] A. Sadat, I. J. Joye, Appl. Sci. 2020, 10, 5918.
- [45] L. Zhang, S. Gopalakrishnan, K. Li, L.-S. Wang, Y. Han, V. M. Rotello, ACS Appl. Mater. Interfaces 2020, 12, 6590.
- [46] J. He, Y. Zhang, Y. Xu, Y. Ma, X. Guo, Foods 2022, 11, 3960.
- [47] L. M. Abbas, G. A.-R. Ahmed, Res. J. Pharm. Biol. 2020, 11, 135.
- [48] S. R. Derkach, D. S. Kolotova, Y. A. Kuchina, N.v. Shumskaya, Polymer 2022, 14, 751.
- [49] J. Valcarcel, J. Fraguas, C. Hermida-Merino, D. Hermida-Merino, M. M. Piñeiro, J. A. Vázquez, Mar. Drugs 2021, 19, 491.
- [50] D. P. Dowling, I. S. Miller, M. Ardhaoui, W. M. Gallagher, J. Biomater. Appl. 2011, 26, 327.
- [51] M. R. Alexander, P. Williams, Biointerphases 2017, 12, 02C201.
- [52] X. Q. Dou, D. Zhang, C. L. Feng, Langmuir 2013, 29, 15359.
- [53] A. N. Lembach, H. B. Tan, I. V. Roisman, T. Gambaryan-Roisman, Y. Zhang, C. Tropea, A. L. Yarin, *Langmuir* 2009, 26, 9516.
- [54] M. Jalili, A. Mozaffari, M. Gashti, M. Parsania, J. Nanoanalysis 2019, 6, 289.
- [55] M. Soltanzadeh, S. H. Peighambardoust, B. Ghanbarzadeh, S. Amjadi, M. Mohammadi, J. M. Lorenzo, H. Hamishehkar, Food Hydrocoll. 2022, 129, 107620.
- [56] W. Janvikul, P. Uppanan, B. Thavornyutikarn, W. Kosorn, P. Kaewkong, *Procedia Eng.* 2013, 59, 158.
- [57] Y. Qian, Z. Zhang, L. Zheng, R. Song, Y. Zhao, J. Nanomater. 2014, 2014, 1.

- [58] J. Dias, P. Bártolo, Procedia CIRP 2013, 5, 216.
- [59] A. L. B. Soares, J. D. D. P. de Moraes, M. A. D'Ávila, F. K. Andrade, R. S. Vieira, *Int. J. Adv. Med. Biotechnol.* 2020, 3, 16.
- [60] Y. Hu, B. Feng, W. Zhang, C. Yan, Q. Yao, C. Shao, F. Yu, F. Li, Y. Fu, Exp. Ther. Med. 2019, 17, 3717.
- [61] W. Fu, Z. Liu, B. Feng, R. Hu, X. He, H. Wang, M. Yin, H. Huang, H. Zhang, W. Wang, Int. J. Nanomedicine 2014, 9, 2335.
- [62] M. Doostmohammadi, H. Forootanfar, M. Shakibaie, M. Torkzadeh-Mahani, H. R. Rahimi, E. Jafari, A. Ameri, A. Ameri, IET Nanobiotechnol. 2021, 15, 277.
- [63] T. Gambaryan-Roisman, Curr. Opin. Colloid Interface Sci. 2014, 19, 320.
- [64] A. B. D. Cassie, S. Baxter, Trans. Faraday Soc. 1944, 40, 546.
- [65] R. N. Wenzel, Ind. Eng. Chem. 1936, 28, 988.

- [66] D. Li, W. Chen, B. Sun, H. Li, T. Wu, Q. Ke, C. Huang, H. El-Hamshary, S. S. Al-Deyab, X. Mo, Colloids Surf. B. Biointerfaces 2016, 146, 632.
- [67] S. Gautam, A. K. Dinda, N. C. Mishra, Mater. Sci. Eng. C 2013, 33, 1228.
- [68] S. R. Gomes, G. Rodrigues, G. G. Martins, C. M. R. Henriques, J. C. Silva, *Mater. Sci. Eng. C* 2013, 33, 1219.

How to cite this article: H. A. Lacy, V. Jenčová, Š. Hauzerová, A. Stanishevsky, *J. Appl. Polym. Sci.* **2023**, e54376. https://doi.org/10.1002/app.54376